EUROPEAN ORGANIZATION FOR NUCLEAR RESEARCH (CERN)

CERN-EP-2024-143
2024/06/07

CMS-EXO-21-017

Search for a resonance decaying to a W boson and a photon in proton-proton collisions at $\sqrt{s} = 13\,\text{TeV}$ using leptonic W boson decays

The CMS Collaboration

Abstract

A search for a new charged particle X with mass between 0.3 and 2.0 TeV decaying to a W boson and a photon is presented, using proton-proton collision data at a center-of-mass energy of 13 TeV, collected by the CMS experiment and corresponding to an integrated luminosity of $138\,\text{fb}^{-1}$. Particle X has electric charge ±1 and is assumed to have spin 0. The search is performed using the electron and muon decays of the W boson. No significant excess above the predicted background is observed. The upper limit at 95% confidence level on the product of the production cross section of the X and its branching fraction to a W boson and a photon is found to be 94 (137) fb for a 0.3 TeV resonance and 0.75 (0.81) fb for a 2.0 TeV resonance, for an X width-to-mass ratio of 0.01% (5%). This search presents the most stringent constraints to date on the existence of such resonances across the probed mass range. A statistical combination with an earlier study based on the hadronic decay mode of the W boson is also performed, and the upper limit at 95% confidence level for a 2.0 TeV resonance is reduced to 0.50 (0.63) fb for an X width-to-mass ratio of 0.01% (5%).

Submitted to the Journal of High Energy Physics

1 Introduction

Many extensions of the standard model (SM) of particle physics, such as unified field theories [1], two Higgs doublet models [2], and folded-supersymmetry models [3], predict the existence of charged resonances decaying to a pair of SM gauge bosons. In this paper, a search for a particle X decaying to a W boson and a photon (Wγ) is presented. Particle X has electric charge ±1 and is assumed to have spin 0. The search utilizes proton-proton (pp) collision data at center-of-mass energy $\sqrt{s} = 13$ TeV delivered by the CERN LHC and collected with the CMS detector in 2016–2018 with a total integrated luminosity of 138 fb^{-1}.

Previous searches for X decaying to Wγ (and Zγ, when it is not possible to distinguish the two massive bosons) have been performed by the ATLAS Collaboration using pp collision data at $\sqrt{s} = 8$ TeV [4] and 13 TeV [5, 6] in leptonic and hadronic final states. Recently, the CMS Collaboration presented a search in the hadronic channel, also using 138 fb^{-1} of 13 TeV data [7]. An excess of events over background expectations was reported near a Wγ resonant mass of 1.58 TeV. The local significance was 2.8 standard deviations assuming a narrow resonance ($\Gamma_X/m_X = 0.01\%$, where Γ_X is the width and m_X is the mass). For a broad ($\Gamma_X/m_X = 5\%$) resonance, the local significance was 3.1 standard deviations. A search for Wγ with leptonic W boson decays, which is both complementary and more sensitive within the range of the reported excess, is the focus of this paper. Additionally, a combination of leptonic and hadronic channels is performed.

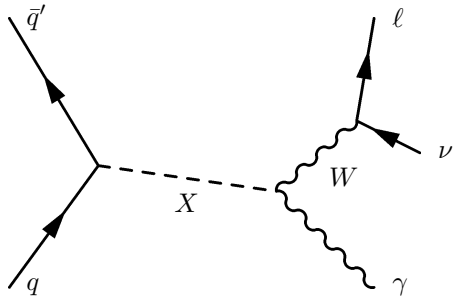

Figure 1: Leading order Feynman diagram for a heavy particle X decaying to a W boson and a photon; the W boson subsequentially decays leptonically.

Figure 1 depicts the leading order (LO) diagram for the production of X with decay to a final state containing a photon γ, a charged lepton ℓ, and a neutrino ν. This search primarily focuses on the W boson decaying to eν and $\mu\nu$. The decays of the W boson to a tau lepton and a neutrino followed by the decay $\tau \to \ell\nu\nu$ ($\ell = \mathrm{e}, \mu$) are also included in the signal sample. Although the branching fraction of the W boson to final states containing eν and $\mu\nu$ is small ($\approx$26% [8]), this search benefits from a reduced background as compared to the hadronic case, especially when studying low-mass resonances. The signature of a ν is the missing transverse momentum $p_{\mathrm{T}}^{\mathrm{miss}}$. Because the longitudinal component of the neutrino momentum cannot be measured or inferred directly, the variable used for the resonance search is the transverse mass m_{T}, defined using only transverse energies and momenta as follows:

$$(m_{\mathrm{T}})^2 = \left(E_{\mathrm{T}}(\gamma) + E_{\mathrm{T}}(\ell) + p_{\mathrm{T}}^{\mathrm{miss}}\right)^2 - |\vec{p}_{\mathrm{T}}(\gamma) + \vec{p}_{\mathrm{T}}(\ell) + \vec{p}_{\mathrm{T}}^{\mathrm{miss}}|^2, \tag{1}$$

where the transverse energy E_{T} is defined as $\sqrt{m^2 + p_{\mathrm{T}}^2}$, $E_{\mathrm{T}}(\gamma)$ is the transverse energy of the photon, $E_{\mathrm{T}}(\ell)$ is the transverse energy of the lepton, $\vec{p}_{\mathrm{T}}(\gamma)$ is the transverse momentum of the photon, and $\vec{p}_{\mathrm{T}}(\ell)$ is the transverse momentum of the charged lepton.

The search results are interpreted in terms of limits on the product of the cross section and the branching fraction to $W\gamma$ within a mass range of 0.3–2.0 TeV for both narrow and broad resonances. The width of the narrow resonance is negligible compared to the 2–7% experimental resolution in the considered mass range. The tabulated results are provided in a HEPData record [9].

2 The CMS detector

The CMS apparatus [10, 11] is a multipurpose, nearly hermetic detector, designed to trigger on [12, 13] and identify electrons, muons, photons, and (charged and neutral) hadrons [14–16]. The central feature of the CMS apparatus is a superconducting solenoid of 6 m internal diameter, providing a magnetic field of 3.8 T. Within the solenoid volume are a silicon pixel and strip tracker, a lead tungstate crystal electromagnetic calorimeter (ECAL), and a brass and scintillator hadron calorimeter (HCAL), each composed of a barrel and two endcap sections. Forward calorimeters extend the pseudorapidity (η) coverage provided by the barrel and endcap detectors. Muons are measured in gas-ionization detectors embedded in the steel flux-return yoke outside the solenoid.

Events of interest are selected using a two-tiered trigger system. The first level (L1), composed of custom hardware processors, uses information from the calorimeters and muon detectors to select events at a rate of around 100 kHz within a fixed latency of 4 μs [13]. The second level, known as the high-level trigger (HLT), consists of a farm of processors running a version of the full event reconstruction software optimized for fast processing, and reduces the event rate to around 1 kHz before data storage [12].

A more detailed description of the CMS detector, together with a definition of the coordinate system used and the relevant kinematic variables, can be found in Ref. [10].

3 Data sets and simulated samples

The data used in this search correspond to a total integrated luminosity of 138 fb^{-1} at $\sqrt{s} =$ 13 TeV and were recorded by the CMS experiment. In years 2016, 2017, and 2018, the data collected correspond to integrated luminosities of 36, 42, and 60 fb^{-1}, respectively [17–19].

The data selection process relies on a combination of triggers. Events containing W bosons that decay to the $e\nu$ final state are selected with an isolated single-electron trigger with a transverse momentum p_T requirement of 27 (32) GeV for 2016 (2017 and 2018). A single-photon trigger with a p_T requirement of 175 (200) GeV for 2016 (2017 and 2018) is also used, to recover events where the electron track is not correctly reconstructed by the HLT software at high p_T, causing the electron to be classified as a photon. The primary trigger for events containing W bosons that decay to the $\mu\nu$ final state requires an isolated muon with a minimum p_T of at least 27 (24) GeV for the 2017 (2016 and 2018) data.

Simulated signal samples are produced at LO in perturbative quantum chromodynamics within a mass range of 0.3–2.0 TeV for both narrow ($\Gamma_X/m_X = 0.01\%$) and broad ($\Gamma_X/m_X = 5\%$) resonances. These samples are employed to calculate the signal efficiency and optimize the analysis selection. The interference with SM $W\gamma$ production is neglected because of its negligible influence on the signal kinematic properties.

The analysis utilizes a background model obtained directly from data. However, simulated background events are used in the analysis optimization and to check the robustness of the

background modeling. The dominant background is the irreducible SM $W\gamma$ process. Other nonnegligible background processes are $Z\gamma$, other SM multi-bosons (e.g., $\gamma\gamma$, WW, WZ, WWγ, and WZγ), V + jets where V is W or Z, γ + jets, $t\bar{t}$, and tW production.

The $t\bar{t}$ and tW processes are generated with POWHEG (v2.0) [20–23], while all the other signal and background events are simulated with MADGRAPH5_aMC@NLO 2.2.2 (2.4.2) [24]. For all simulated samples, the pp interaction simulation is supplemented with NNPDF3.0 NLO [25] (NNPDF3.1 NNLO [26]) parton distribution functions (PDFs) for 2016 (2017 and 2018) conditions. The event generator PYTHIA 8.205 (8.230) [27] is used to simulate fragmentation, parton showering, and hadronization, with the CUETP8M1 [28, 29] (CP5 [30]) underlying event tune for 2016 (2017 and 2018) samples.

All simulated samples are processed with the full CMS detector model based on GEANT4 [31]. The instantaneous luminosity delivered by the LHC results in additional pp interactions in the same or neighboring bunch crossings, known as pileup. The average number of pileup interactions in the 2016 (2017 and 2018) data set is about 23 (32). Pileup effects are taken into account by superimposing simulated minimum bias events on the hard scattering interaction, with a multiplicity distribution reweighted to match that observed in the data [32].

4 Event reconstruction

The particle-flow (PF) algorithm is a global event reconstruction technique [33] that aims to reconstruct and identify every particle in an event, with an optimized combination of information from the various elements of the CMS detector, as a PF candidate.

Electrons are reconstructed by geometrically matching charged-particle tracks from the tracking system with energy clusters deposited in the ECAL. The reconstruction efficiency is higher than 95% for $E_T > 20$ GeV [14]. The electron momentum is evaluated by combining the energy measurement in the ECAL with the momentum measurement in the tracker. The momentum resolution for electrons with p_T of $\approx$45 GeV from $Z \to ee$ decays is 1.7–4.5%. It is generally better in the barrel region than in the endcaps, and it also depends on the bremsstrahlung energy emitted by the electron as it traverses the material in front of the ECAL [14].

Muons are reconstructed from compatible tracks in the inner tracker and the muon detectors [15]. They are measured in the pseudorapidity range $|\eta| < 2.4$ with detection planes made using three technologies: drift tubes, cathode strip chambers, and resistive-plate chambers. The single-muon trigger efficiency exceeds 90% over the full η range, and the efficiency to reconstruct and identify muons is greater than 96%. The momenta of muons are obtained from the curvature of their corresponding tracks. Matching muons to tracks measured in the silicon tracker results in a relative p_T resolution, for muons with p_T up to 100 GeV, of 1% in the barrel and 3% in the endcaps. The p_T resolution in the barrel is better than 7% for muons with p_T up to 1 TeV [15].

The energies of photons are obtained from ECAL measurements. In the barrel section of the ECAL, an energy resolution of about 1% is achieved for unconverted or late-converting photons in the tens of GeV energy range. The energy resolution of the remaining barrel photons is about 1.3% up to $|\eta| = 1$, increasing to about 2.5% at $|\eta| = 1.4$. In the endcaps, the energy resolution is about 2.5% for unconverted or late-converting photons and is 3–4% for all others [34].

The energies of charged hadrons are determined from a combination of their momenta measured in the tracker and their corresponding ECAL and HCAL energy deposits, which are corrected for the response function of the calorimeters to hadronic showers. Finally, the energies

of neutral hadrons are obtained from the corresponding corrected ECAL and HCAL energies.

Jets are clustered from PF candidates using the anti-k_T algorithm [35, 36] with a distance parameter of 0.4. Jets found within $\Delta R \equiv \sqrt{(\Delta\eta)^2 + (\Delta\phi)^2} = 0.4$ from an identified muon, electron, or photon are removed, where ϕ is the azimuthal angle. Jet flavor tagging is performed using the DEEPJET [37] tagger at the medium working point. DEEPJET is a multi-class flavor tagger algorithm that combines information from charged and neutral PF candidates, reconstructed secondary vertices, and global variables using a deep neural network [37, 38]. The medium working point is characterized by a 1% misidentification probability for light-quark or gluon jets and an efficiency of 80% for tagging jets originating from a b quark. Rejecting events with a b jet passing the medium working point reduces the $\mathrm{t\bar{t}}$ backgrounds significantly.

The missing transverse momentum vector $\vec{p}_{\mathrm{T}}^{\,\mathrm{miss}}$ is computed as the negative vector sum of the transverse momenta of all the PF candidates in an event, and its magnitude is denoted as $p_{\mathrm{T}}^{\mathrm{miss}}$ [39]. The $\vec{p}_{\mathrm{T}}^{\,\mathrm{miss}}$ is modified to account for corrections to the energy scale of the reconstructed jets in the event.

The primary vertex (PV) is taken to be the vertex corresponding to the hardest scattering in the event, evaluated using tracking information alone, as described in Section 9.4.1 of Ref. [40].

5 Event selection

Events are selected in two steps. A basic selection is applied with loose lepton and photon selection criteria to veto backgrounds with multiple leptons and photons. Then a tighter event selection is applied to improve the signal sensitivity.

In the basic selection, candidate electrons, muons, and photons are selected using the standard CMS "medium" photon and electron and "tight" muon identification (ID) requirements [14, 15]. Many of the kinematic variable thresholds are the same for both lepton channels because their signal kinematic distributions and background compositions are very similar.

Leptons are required to have $p_{\mathrm{T}} > 10\,\mathrm{GeV}$, and photons $p_{\mathrm{T}} > 15\,\mathrm{GeV}$. Leptons are also required to satisfy η selections to ensure they are in the regions of the detector where they will be well measured. Since the leptons from the signal process are typically isolated, backgrounds from jets being misidentified as an electron are reduced by requirements on $\mathcal{I}_{\mathrm{PF,rel}}$, defined as the summed p_{T} of reconstructed PF candidates within a cone centered on the electron momentum vector divided by the electron p_{T}. Similar isolation criteria are integrated into the CMS standard muon and photon identification requirements. Leptons and photons must be separated by $\Delta R > 0.4$. These kinematic and identification requirements are referred to as the "basic object selections" and are summarized in Table 1. Leptons and photons passing these requirements are referred to as basic electrons, muons, and photons later.

To reduce backgrounds from $\mathrm{t\bar{t}}$ and multi-boson processes, events with more than one lepton or photon passing the basic requirements are rejected.

To further reduce backgrounds, an optimization is performed on additional kinematic variables. The selected electron and muon are required to match the trigger object that caused the event to be selected by the HLT. The lepton p_{T} requirements are increased to 35 (30) GeV in the electron (muon) channels to exclude events near the trigger threshold where the trigger efficiency changes significantly. The CMS standard "tight" identification requirement on the electron is used [14]. A threshold of 40 GeV on $p_{\mathrm{T}}^{\mathrm{miss}}$ is required in both channels.

For the signal, there is an approximately linear relationship between $p_{\mathrm{T}}(\gamma)$ and m_{T}. This

Table 1: Basic object selection requirements. Definitions are described in more detail in the text.

Selection	Electron	Muon	Photon
p_T	>10 GeV	>10 GeV	>15 GeV
η	$\lvert\eta\rvert < 1.44$ or $1.57 < \lvert\eta\rvert < 2.1$	$\lvert\eta\rvert < 2.4$	$\lvert\eta\rvert < 1.44$ or $1.57 < \lvert\eta\rvert < 2.5$
ID	Medium	Tight	Medium
Isolation	Integrated with ID	$\mathcal{I}_{\text{PF,rel}} < 0.15$	Integrated with ID
ΔR	$\Delta R(\gamma, e) > 0.4$	$\Delta R(\gamma, \mu) > 0.4$	$\Delta R(\gamma, e) > 0.4$ and $\Delta R(\gamma, \mu) > 0.4$

feature can be used to select signal-like events and reject background-like ones. Requiring $p_T(\gamma) > 0.4\, m_T$ rejects SM Wγ process events, which generally tend to have a softer $p_T(\gamma)$ spectrum, while requiring $p_T(\gamma) < 0.55\, m_T$ preferentially rejects $t\bar{t}$ events. These m_T-dependent $p_T(\gamma)$ selection cuts achieve a background rejection of more than 55% while preserving about 90% of signal events. The requirement on the photon pseudorapidity is also tightened to $\lvert\eta\rvert < 1.44$, thus selecting only photons reconstructed in the barrel section of the calorimeters. To further reject $t\bar{t}$ backgrounds, events containing b-tagged jets passing the medium working point of the DEEPJET tagger are rejected.

In the electron channel, to suppress $Z \to ee$ events where one of the electrons is mistakenly reconstructed as a photon, a pixel detector seed veto (PSV), which rejects photon candidates with more than two hits in the pixel detector, is applied [14]. The contribution of this process is further reduced by rejecting events where the invariant mass of the electron and photon is near the Z boson mass—specifically between 71 and 111 GeV, corresponding to roughly ± 5 widths of a reconstructed Z boson peak. These selections are summarized in Table 2.

Table 2: Event selection requirements for the electron and the muon channels. Definitions are described in more detail in the text.

Selection	Electron channel	Muon channel
e/μ sel.	$p_T(e) > 35$ GeV and tight ID	$p_T(\mu) > 30$ GeV and tight ID
p_T^{miss}	>40 GeV	
γ sel.	$0.4\, m_T < p_T(\gamma) < 0.55\, m_T$ and $\lvert\eta\rvert < 1.44$	
Z veto	$\lvert m_{e\gamma} - 91.0\rvert > 20$ GeV and PSV	—
b veto	No medium b-tagged jets	

Signal efficiencies estimated from the simulation of leptonically decaying W bosons are shown in Fig. 2. Events in the first bin require exactly one reconstructed basic electron or muon and one photon, satisfying the selection criteria reported in Table 1. The next bin contains events satisfying the HLT, and the subsequent bins have the selections listed in Table 2 applied sequentially. The tight photon selections, which are necessary to reduce the backgrounds, have the largest impact on the efficiency. The narrow (0.01%) and broad (5%) resonances exhibit similar efficiencies within the displayed mass range. Events containing W bosons that decay to the $\tau\nu$ final state with τ subsequently decaying to e or μ are considered as signal and included in the acceptance. They constitute about 10% of the selected events.

Signal efficiencies for all simulated signal samples, separately for the electron and muon channels, are shown in Fig. 3. The product of detector acceptances and analysis selection efficiencies are shown at three consecutive stages: event reconstruction, HLT, and final signal selection. The total signal efficiency ranges from 3.4 (4.8)% to 12.7 (13.9)% for the electron (muon) channel. The efficiency increases with m_X. The efficiencies for the electron channel are generally 1–2% lower than those for the muon channel.

The merged distributions from the electron and muon channels for m_T and $p_T(\gamma)$ are shown

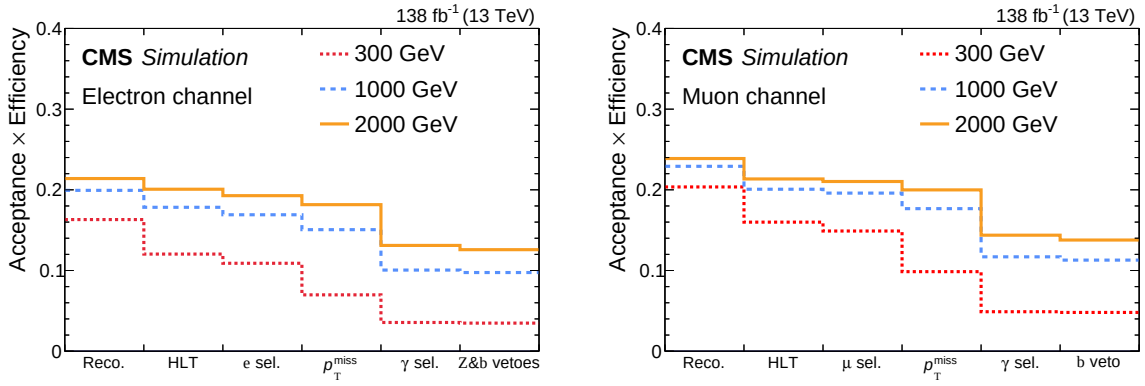

Figure 2: Product of detector acceptance and analysis selections efficiency for different particle mass assumptions—300, 1000, and 2000 GeV, in red, blue, and orange, respectively—to pass sequential requirements in the broad-width case. The narrow-width case is similar. The first bin represents selecting events with exactly one reconstructed basic electron or muon and one photon, satisfying the selection criteria reported in Table 1. The next bin contains events satisfying the HLT, and the subsequent bins have the selections listed in Table 2 applied sequentially. The left (right) plot is for the electron (muon) channel.

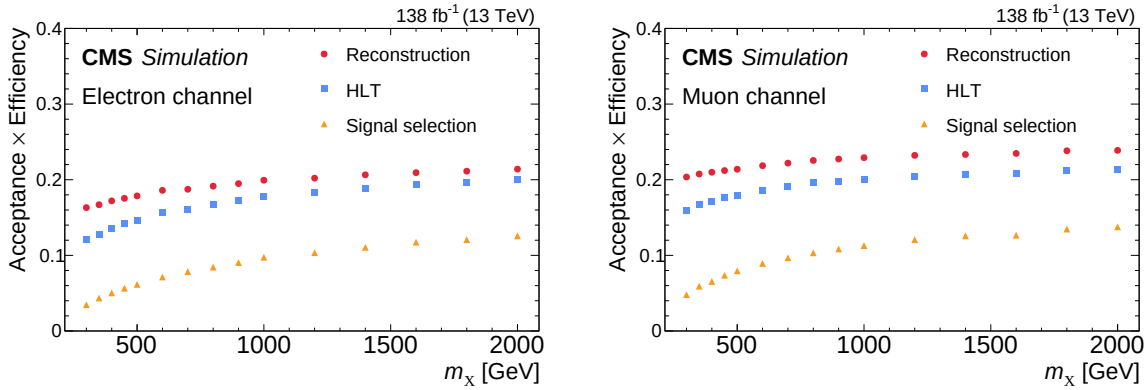

Figure 3: Product of detector acceptance and analysis selection efficiency in the electron (left) and muon (right) channel as functions of the particle X mass in the broad-width case. The narrow-width case is similar. Three analysis requirements are applied consecutively: event reconstruction, HLT, and final signal selection. The product of detector acceptance and analysis selection efficiencies are shown at each stage in red, blue, and orange, respectively.

in Fig. 4. The observed data are consistent with the background expectation from simulation. The dominant background is the SM Vγ process (where V is W or Z), followed by V/γ + jets (V + jets, γ + jets), and top ($t\bar{t}$, tW) backgrounds. Other background sources contributing to the distributions are grouped under the label "Other".

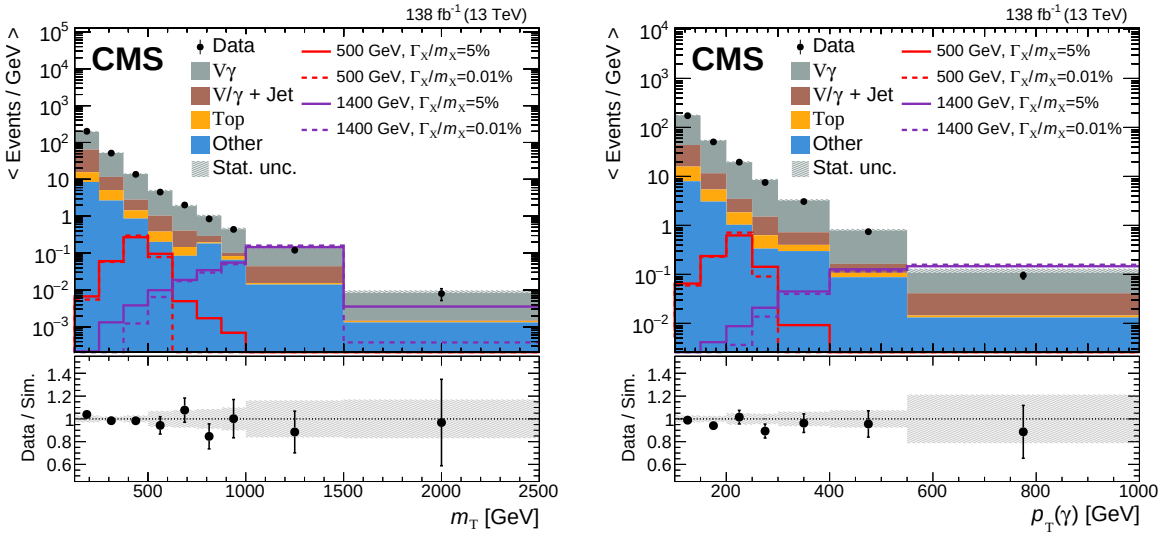

Figure 4: Distributions of m_T (left) and $p_T(\gamma)$ (right) from simulation (stacked histograms) and data events (black points) passing all analysis selections. The number of events is divided by the width of each individual bin. The simulation distributions agree with data within statistical uncertainty. Four signal distributions, with two mass assumptions and two width assumptions, are also overlaid (dashed and solid lines). Each signal is plotted with a total cross section of 3 fb. Because of the limited number of simulated events, in the high mass region, progressively larger bin sizes are used. The last bin includes the overflow events. The lower panel shows the ratio of data to simulation.

6 Signal and background modeling

The m_T distributions from simulations corresponding to the three data-taking periods (i.e., 2016, 2017, and 2018) are similar, with only minor variations reflecting the differences in the modeling of the pileup, the trigger requirements, and the detector performance. To reduce the signal modeling uncertainties, the simulated signal samples from the three data-taking periods are combined. The resulting distribution is fit with a double-sided Crystal Ball (DSCB) function [41, 42]. This six-parameter function has a central core with a Gaussian distribution characterized by two parameters: mean transverse mass $\overline{m_T}$ and resolution σ_{m_T}. The m_T distribution obtained from this combined fit is consistent with that obtained from each of the three individual data-taking periods.

The background simulation samples shown in Fig. 4 play a crucial role in our selection optimization and provide insights into the underlying processes. However, the background estimation does not rely on the simulation. Instead, it is modeled analytically via a fit to the data using functions described below:

$$p_0 x^{\sum_{i=1}^{N} p_i \log^{i-1}(x)}, \tag{2}$$

$$p_0 \frac{(1-x)^{p_1}}{x^{\sum_{i=2}^{N} p_i \log^{i-2}(x)}}, \tag{3}$$

$$p_0 e^{p_1 x} x^{\sum_{i=2}^{N} p_i \log^{i-2}(x)}, \tag{4}$$

where x is $m_T/\sqrt{s}$. The parameters p_i vary freely in the fit, and the index i ranges up to the order N of each function. These functions are commonly used in similar searches [4–7]. The number of free parameters in each functional form is determined using a Fisher F-test [43]. In all data-taking years and lepton channels, the number of parameters determined by this procedure is either three or four. To increase the flexibility of the background modeling, a discrete profiling method [44] is employed to consider all functions when performing the ultimate fit to the data. This approach optimizes the background parameters of each function independently to determine which function represents the background best.

The fit to the data with the background-only hypothesis is shown in Fig. 5 for both the electron and the muon channels. The fit parameters have no correlation among the years and all are set to be freely floating. This smooth background parametrization provides an adequate description of the data over the entire mass range probed.

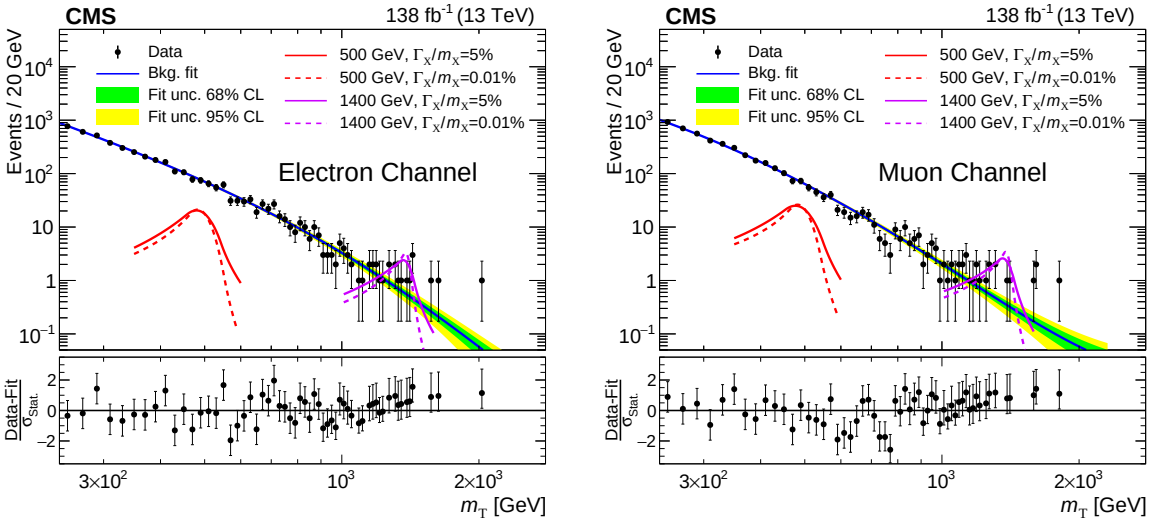

Figure 5: Background-only fit to data (black points) with the fitted background model shown as a blue line. The green (inner) and yellow (outer) bands show, respectively, the 68% and 95% confidence level statistical uncertainties in the fitted model. Four signal models are also overlaid. Their total cross sections are set to the expected limits at 95% confidence level from this search with leptonic decays of the W boson. There are two mass assumptions—500 and 1400 GeV, in red and magenta, respectively—and two width assumptions—narrow (solid curves) and broad (dashed curves). The lower panel contains the pull distribution, defined as the difference between the data yield and the background prediction divided by their combined uncertainty. The left (right) panel is the electron (muon) channel with all three years' data combined.

7 Systematic uncertainties

Systematic uncertainties affect both the normalization and shape of the signal distributions. They are included in the fit in the form of log-normal (normalization uncertainty) or Gaussian (shape uncertainty) priors for the nuisance parameters.

The primary systematic uncertainties in the signal normalization are uncertainties on the integrated luminosity, the PDFs, the choices of renormalization and factorization scales, the lepton

trigger and identification efficiencies, the photon identification efficiency, the pileup description, the b tagging efficiency, and an ECAL trigger mistiming correction [13]. These systematic uncertainties increase for higher resonance masses and are independent of the width-to-mass ratio.

Lepton and photon identification and reconstruction: uncertainties arising from lepton identification and reconstruction criteria, as well as trigger efficiencies, are included as normalization uncertainties. Muon-related uncertainties range from 0.5 to 1.2% [15], while electron-related uncertainties are higher, spanning from 1.5 to 3.8% [14]. The photon identification uncertainty is significant in both the electron and muon channels. It is included as a normalization uncertainty, ranging from 1.4 to 5.2% [14].

Integrated luminosity: the integrated luminosities for the 2016, 2017, and 2018 data-taking years have 1.2–2.5% individual uncertainties [17–19], while the overall uncertainty for the 2016–2018 period is 1.6%. These are included as normalization uncertainties.

Renormalization/factorization scales and PDFs: theoretical uncertainties arise from the choice of the renormalization and factorization scales in the matrix elements calculation and the proton PDFs. These uncertainties are estimated by varying the renormalization and factorization scales independently by factors of 0.5 and 2, excluding the extreme cases (0.5,2) and (2,0.5), and assessing the uncertainty to be the largest difference from the nominal distribution of m_{T} of the signal. Additionally, signal distributions are generated using different sets of NNPDF3.1 [25, 26] replicas to account for the PDF uncertainties. The combined uncertainty from these sources varies from 1.9 to 4.4% as normalization uncertainties.

Minor uncertainties: systematic uncertainty from pileup reweighting is quantified by varying the total inelastic cross section within its $\pm 5\%$ uncertainty range [32]. The data-to-simulation ratios of the b jet tagging efficiency and misidentification probability are used to apply event weights to simulated samples. The uncertainties on these ratios result in uncertainties on the weights, from which systematic uncertainties are inferred. These sources, as well as the ECAL trigger mistiming correction uncertainty [13] and jet energy scale and resolution uncertainties, contribute less than 1% to the signal normalization uncertainty.

A summary of the systematic uncertainties affecting the signal normalization is shown in Fig. 6 for each lepton channel separately. Uncertainties are divided into five categories: photon-related, lepton-related, theoretical, integrated luminosity, and all other uncertainties (shown as "Other"). Their quadrature summation is also included ("Total"). Driven by the increased photon-related uncertainty, the relative signal yield uncertainty grows from 3.2 (2.9) to 8.3 (6.7)% for resonance masses from 300 GeV to 2 TeV, in the electron (muon) channel. The narrow and broad resonances have similar values for all uncertainties. All uncertainties are correlated between the electron and muon channels with the exception of lepton-related uncertainties.

The signal distribution, modeled by the DSCB function, is primarily characterized by two important parameters from the Gaussian distribution part: the mean transverse mass $\overline{m_{\mathrm{T}}}$ and resolution $\sigma_{m_{\mathrm{T}}}$. These parameters are correlated across years for each resonance mass. Uncertainties in lepton, photon, and jet energy scales and resolutions can affect the shape of the signal distribution. Their effect is included in the fit as an additional uncertainty in $\overline{m_{\mathrm{T}}}$ and $\sigma_{m_{\mathrm{T}}}$ that varies as a function of the resonance mass.

To assess the effects of systematic uncertainties in these parameters, alternative signal m_{T} distributions are generated by varying the fundamental kinematic quantities, e.g., photon p_{T}, lepton p_{T}, etc., within their systematic uncertainty and reevaluating m_{T} for each event. The difference in the resulting signal fit parameters $\overline{m_{\mathrm{T}}}$ and $\sigma_{m_{\mathrm{T}}}$ are taken as one-standard-deviation uncer-

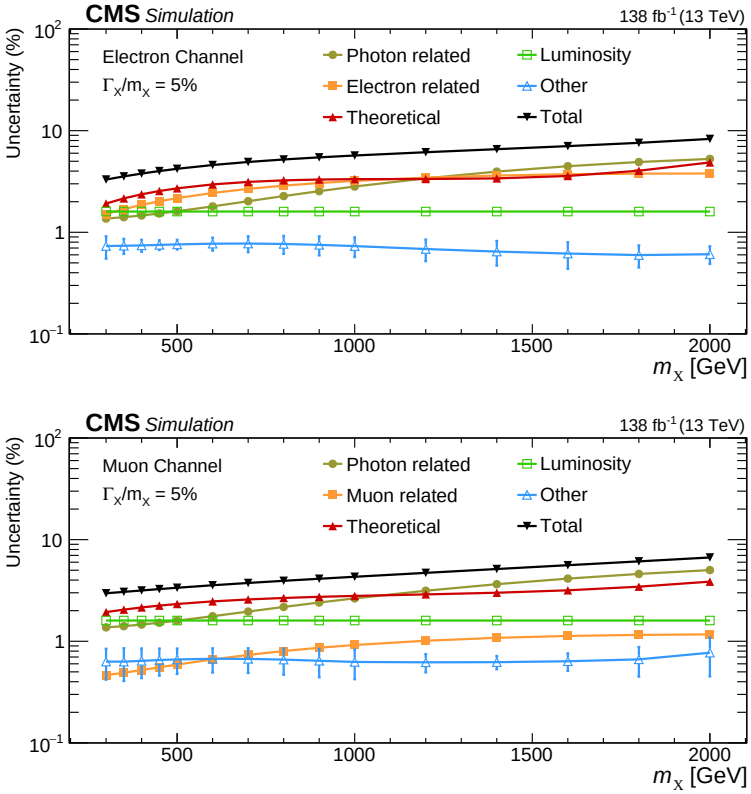

Figure 6: Systematic uncertainties affecting the signal normalization in the electron (upper) and muon (lower) channels for the broad resonance are shown. Error bars represent the asymmetric uncertainties (downward and upward variations), with the central value representing the average uncertainty. The total systematic uncertainty (black) increases steadily with the resonant mass assumption. The uncertainties for the narrow-width case are nearly identical.

tainties. All of these uncertainties are combined in quadrature, and their combined effect is much smaller than the normalization uncertainties. In most cases, the total uncertainty is predominantly driven by the variation in the photon energy scale. The uncertainty in $\overline{m_{\mathrm{T}}}$ is 0.3% at the lowest considered mass and 1.9% at the highest, while the uncertainty in $\sigma_{m_{\mathrm{T}}}$ varies from 3 to 7 (3 to 4)% for narrow (broad) resonance signals.

As previously described in Section 6, we treat the normalization and shape of the background distribution as free parameters and evaluate them during the fit to the data. These parameters are individually evaluated for each signal mass and width hypothesis and are not correlated from year to year.

A dedicated study focused on systematic effects affecting the background shape is conducted to confirm that no systematic bias on the signal extraction is present. Pseudo-data are generated from the background model to produce many m_{T} spectra—some containing signal and others without. Each of these spectra is fit in the same fashion as the data using the nominal discrete-profiling background model. During these fits, both the signal strengths and the background normalizations are allowed to vary freely. All distributions of fitted signal strength minus injected signal strength divided by the signal strength uncertainty—typically called a "pull" distribution—are centered around zero and have width of unity. Therefore, any potential systematic bias arising from our background fitting procedure is negligible compared to the statistical uncertainties inherent in the fit. This analysis is dominated by statistical uncertainties; the overall impact of the systematic uncertainties is small.

8 Results

No signal-like excess of events above background expectations is observed. Model-specific upper limits are set on the product of the X production cross section and its branching fraction to $\mathrm{W}\gamma$ for both the narrow and broad resonance scenarios. We determine these limits with the $\mathrm{CL_s}$ method [45–47] and the asymptotic approximation [48] using the CMS statistical analysis tool COMBINE [49]. The test statistic is derived from a likelihood ratio within the asymptotic approximation.

Systematic uncertainties are incorporated into the likelihood model as penalty terms with nuisance parameters. All nuisance parameters are fully correlated across the years with the exception of the integrated luminosity uncertainty, the ECAL trigger mistiming correction, and the background distribution parameters.

Figure 7 shows the expected and observed limits on $\sigma\mathcal{B}(X \to \mathrm{W}\gamma)$ at 95% confidence level (CL) for both the narrow- and broad-width resonance hypotheses. The limits for the narrow-width resonance hypothesis are 15% to 20% better than the ones for the broad-width resonance hypothesis.

An earlier study based on the hadronic decay mode of the W boson using the same 13 TeV data sample [7] identified a small excess of events over background expectations near a $\mathrm{W}\gamma$ resonance mass of 1.58 TeV, with 2.8 (3.1) standard deviations of local significance for the narrow (broad) signal hypotheses. The event selections of this search and the previous one are orthogonal; only the integrated luminosity uncertainties are correlated. In this search, the largest local significance for the narrow (broad) signal hypotheses is 1.7 (1.6) standard deviations. The combined limits on $\sigma\mathcal{B}(\mathrm{X} \to \mathrm{W}\gamma)$ are shown in Fig. 8. The local p-values for the background-only fit are presented in Fig. 9, with the left (right) plot showing the results for the narrow (broad) resonance hypothesis. Both separate and combined p-values are shown over the common mass

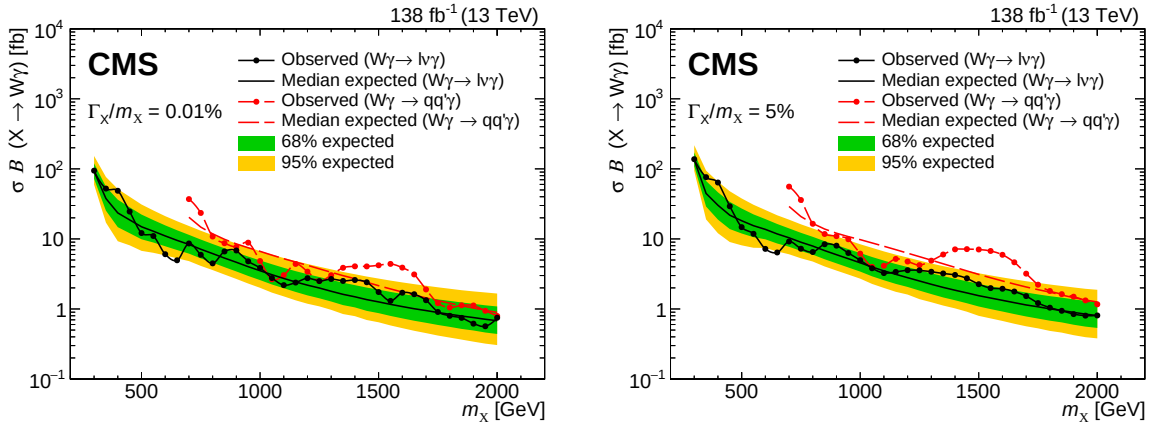

Figure 7: Expected and observed limits at 95% CL on $\sigma\mathcal{B}(X \to W\gamma)$ from events with leptonic decays (solid black lines) of the W boson as a function of the X resonant mass. The limits from the hadronic decays (dashed red lines) of the W boson are taken from [7] and included for comparison. The results for the narrow (broad) width assumption are shown on the left (right).

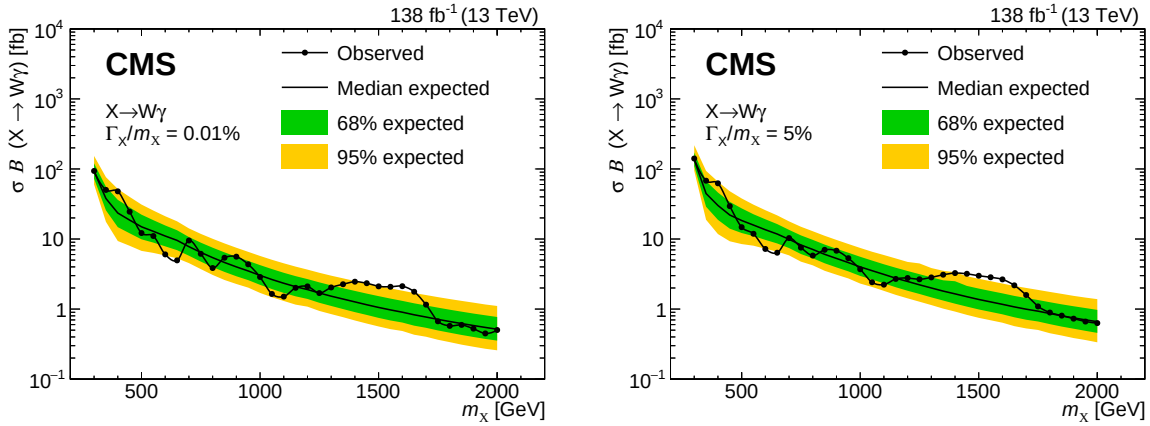

Figure 8: Expected and observed limits at 95% CL on $\sigma\mathcal{B}(X \to W\gamma)$ utilizing both hadronic (from [7]) and leptonic (this analysis) W decays as a function of the X resonant mass. The results for the narrow (broad) width assumption are shown on the left (right).

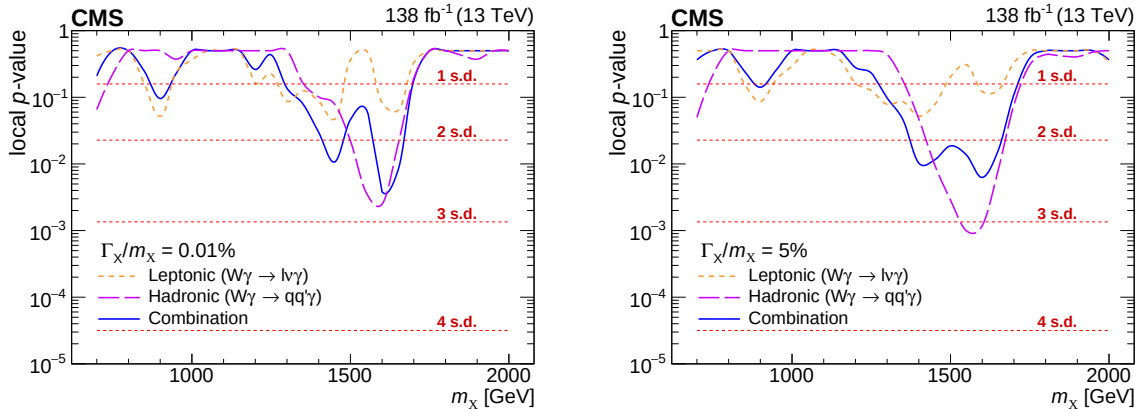

Figure 9: Observed local p-values for narrow (left) and broad (right) resonance width hypotheses with the background-only fit in the hadronic (from [7]) and leptonic (this analysis) channels. The blue line shows the observed local p-values after their combination. In the hadronic channel (violet line), the largest excess corresponds to a local significance of 2.8 (3.1) standard deviations (s.d.) for narrow (broad) signals. In the leptonic channel (orange line), the largest local significance is 1.7 (1.6) standard deviations. After combining with the leptonic channel, the largest excess is 2.7 (2.5) standard deviations.

range. The maximal excess observed in the earlier study is reduced to 2.7 (2.5) standard deviations of local significance for the narrow (broad) signal hypotheses.

9 Summary

This study presents a search for a new particle X decaying into a W boson and a photon with mass hypotheses from 0.3 to 2.0 TeV and X width-to-mass ratio hypotheses of 0.01% (narrow) and 5% (broad). Events with a muon or an electron, large $p_{\mathrm{T}}^{\mathrm{miss}}$, and a high-$p_{\mathrm{T}}$ photon are analyzed. The transverse mass of the lepton, photon, and $p_{\mathrm{T}}^{\mathrm{miss}}$ is the primary kinematic observable. The search utilizes proton-proton collision data collected at a center-of-mass energy of 13 TeV with the CMS detector at the LHC throughout 2016–2018, corresponding to an integrated luminosity of 138 fb^{-1}.

This search reveals no statistically significant excess of events above the background. Upper limits at the 95% confidence level on the product of the cross section and branching fraction for Wγ resonances are set. These limits span a range from 94 (137) to 0.75 (0.81) fb for the narrow (broad) resonance hypothesis. These findings represent the most stringent constraints to date on the existence of such resonances across the probed mass range.

This search complements an earlier study based on the hadronic decay mode of the W boson using the full 13 TeV data sample [7]. By combining searches for both leptonic and hadronic decays of W bosons, the largest local excess seen in the hadronic channel is reduced from 3.1 to 2.5 standard deviations for the broad signal-width hypothesis. The upper limit at the 95% confidence level at 2 TeV is reduced from 0.75 (0.81) to 0.50 (0.63) fb for the narrow (broad) resonance hypothesis.

Acknowledgments

We congratulate our colleagues in the CERN accelerator departments for the excellent performance of the LHC and thank the technical and administrative staffs at CERN and at other

CMS institutes for their contributions to the success of the CMS effort. In addition, we gratefully acknowledge the computing centers and personnel of the Worldwide LHC Computing Grid and other centers for delivering so effectively the computing infrastructure essential to our analyses. Finally, we acknowledge the enduring support for the construction and operation of the LHC, the CMS detector, and the supporting computing infrastructure provided by the following funding agencies: SC (Armenia), BMBWF and FWF (Austria); FNRS and FWO (Belgium); CNPq, CAPES, FAPERJ, FAPERGS, and FAPESP (Brazil); MES and BNSF (Bulgaria); CERN; CAS, MoST, and NSFC (China); MINCIENCIAS (Colombia); MSES and CSF (Croatia); RIF (Cyprus); SENESCYT (Ecuador); ERC PRG, RVTT3 and MoER TK202 (Estonia); Academy of Finland, MEC, and HIP (Finland); CEA and CNRS/IN2P3 (France); SRNSF (Georgia); BMBF, DFG, and HGF (Germany); GSRI (Greece); NKFIH (Hungary); DAE and DST (India); IPM (Iran); SFI (Ireland); INFN (Italy); MSIP and NRF (Republic of Korea); MES (Latvia); LMTLT (Lithuania); MOE and UM (Malaysia); BUAP, CINVESTAV, CONACYT, LNS, SEP, and UASLP-FAI (Mexico); MOS (Montenegro); MBIE (New Zealand); PAEC (Pakistan); MES and NSC (Poland); FCT (Portugal); MESTD (Serbia); MCIN/AEI and PCTI (Spain); MOSTR (Sri Lanka); Swiss Funding Agencies (Switzerland); MST (Taipei); MHESI and NSTDA (Thailand); TUBITAK and TENMAK (Turkey); NASU (Ukraine); STFC (United Kingdom); DOE and NSF (USA).

Individuals have received support from the Marie-Curie program and the European Research Council and Horizon 2020 Grant, contract Nos. 675440, 724704, 752730, 758316, 765710, 824093, 101115353, 101002207, and COST Action CA16108 (European Union); the Leventis Foundation; the Alfred P. Sloan Foundation; the Alexander von Humboldt Foundation; the Science Committee, project no. 22rl-037 (Armenia); the Belgian Federal Science Policy Office; the Fonds pour la Formation à la Recherche dans l'Industrie et dans l'Agriculture (FRIA-Belgium); the Agentschap voor Innovatie door Wetenschap en Technologie (IWT-Belgium); the F.R.S.-FNRS and FWO (Belgium) under the "Excellence of Science – EOS" – be.h project n. 30820817; the Beijing Municipal Science & Technology Commission, No. Z191100007219010 and Fundamental Research Funds for the Central Universities (China); the Ministry of Education, Youth and Sports (MEYS) of the Czech Republic; the Shota Rustaveli National Science Foundation, grant FR-22-985 (Georgia); the Deutsche Forschungsgemeinschaft (DFG), under Germany's Excellence Strategy – EXC 2121 "Quantum Universe" – 390833306, and under project number 400140256 - GRK2497; the Hellenic Foundation for Research and Innovation (HFRI), Project Number 2288 (Greece); the Hungarian Academy of Sciences, the New National Excellence Program - ÚNKP, the NKFIH research grants K 131991, K 133046, K 138136, K 143460, K 143477, K 146913, K 146914, K 147048, 2020-2.2.1-ED-2021-00181, and TKP2021-NKTA-64 (Hungary); the Council of Science and Industrial Research, India; ICSC – National Research Center for High Performance Computing, Big Data and Quantum Computing and FAIR – Future Artificial Intelligence Research, funded by the NextGenerationEU program (Italy); the Latvian Council of Science; the Ministry of Education and Science, project no. 2022/WK/14, and the National Science Center, contracts Opus 2021/41/B/ST2/01369 and 2021/43/B/ST2/01552 (Poland); the Fundação para a Ciência e a Tecnologia, grant CEECIND/01334/2018 (Portugal); the National Priorities Research Program by Qatar National Research Fund; MCIN/AEI/10.13039/501100011033, ERDF "a way of making Europe", and the Programa Estatal de Fomento de la Investigación Científica y Técnica de Excelencia María de Maeztu, grant MDM-2017-0765 and Programa Severo Ochoa del Principado de Asturias (Spain); the Chulalongkorn Academic into Its 2nd Century Project Advancement Project, and the National Science, Research and Innovation Fund via the Program Management Unit for Human Resources & Institutional Development, Research and Innovation, grant B37G660013 (Thailand); the Kavli Foundation; the Nvidia Corporation; the SuperMicro Corporation; the

Welch Foundation, contract C-1845; and the Weston Havens Foundation (USA).

References

[1] N. Arkani-Hamed, R. T. D'Agnolo, M. Low, and D. Pinner, "Unification and new particles at the LHC", *JHEP* **11** (2016) 082, doi:10.1007/JHEP11(2016)082, arXiv:1608.01675.

[2] H. E. Logan and Y. Wu, "Searching for the Wγ decay of a charged Higgs boson", *JHEP* **11** (2018) 121, doi:10.1007/JHEP11(2018)121, arXiv:1809.09127.

[3] G. Burdman et al., "Colorless top partners, a 125 GeV Higgs boson, and the limits on naturalness", *Phys. Rev. D* **91** (2015) 055007, doi:10.1103/PhysRevD.91.055007, arXiv:1411.3310.

[4] ATLAS Collaboration, "Search for new resonances in Wγ and Zγ final states in pp collisions at $\sqrt{s} = 8$ TeV with the ATLAS detector", *Phys. Lett. B* **738** (2014) 428, doi:10.1016/j.physletb.2014.10.002, arXiv:1407.8150.

[5] ATLAS Collaboration, "Search for heavy resonances decaying to a photon and a hadronically decaying Z/W/H boson in pp collisions at $\sqrt{s} = 13$ TeV with the ATLAS detector", *Phys. Rev. D* **98** (2018) 032015, doi:10.1103/PhysRevD.98.032015, arXiv:1805.01908.

[6] ATLAS Collaboration, "Search for high-mass Wγ and Zγ resonances using hadronic W/Z boson decays from 139 fb^{-1} of pp collisions at $\sqrt{s}$ = 13 TeV with the ATLAS detector", *JHEP* **07** (2023) 125, doi:10.1007/JHEP07(2023)125, arXiv:2304.11962.

[7] CMS Collaboration, "Search for Wγ resonances in proton-proton collisions at $\sqrt{s} = 13$ TeV using hadronic decays of Lorentz-boosted W bosons", *Phys. Lett. B* **826** (2022) 136888, doi:10.1016/j.physletb.2022.136888, arXiv:2106.10509.

[8] Particle Data Group, R. L. Workman et al., "Review of Particle Physics", *PTEP* **2022** (2022) 083C01, doi:10.1093/ptep/ptac097.

[9] "HEPData record for this analysis", 2024. doi:10.17182/hepdata.152436.

[10] CMS Collaboration, "The CMS experiment at the CERN LHC", *JINST* **3** (2008) S08004, doi:10.1088/1748-0221/3/08/S08004.

[11] CMS Collaboration, "Development of the CMS detector for the CERN LHC Run 3", 2023. arXiv:2309.05466. Accepted by *JINST*.

[12] CMS Collaboration, "The CMS trigger system", *JINST* **12** (2017) P01020, doi:10.1088/1748-0221/12/01/P01020, arXiv:1609.02366.

[13] CMS Collaboration, "Performance of the CMS level-1 trigger in proton-proton collisions at $\sqrt{s} = 13$ TeV", *JINST* **15** (2020) P10017, doi:10.1088/1748-0221/15/10/P10017, arXiv:2006.10165.

[14] CMS Collaboration, "Electron and photon reconstruction and identification with the CMS experiment at the CERN LHC", *JINST* **16** (2021) P05014, doi:10.1088/1748-0221/16/05/P05014, arXiv:2012.06888.

[15] CMS Collaboration, "Performance of the CMS muon detector and muon reconstruction with proton-proton collisions at $\sqrt{s} = 13$ TeV", *JINST* **13** (2018) P06015, doi:10.1088/1748-0221/13/06/P06015, arXiv:1804.04528.

[16] CMS Collaboration, "Description and performance of track and primary-vertex reconstruction with the CMS tracker", *JINST* **9** (2014) P10009, doi:10.1088/1748-0221/9/10/P10009, arXiv:1405.6569.

[17] CMS Collaboration, "Precision luminosity measurement in proton-proton collisions at $\sqrt{s} = 13$ TeV in 2015 and 2016 at CMS", *Eur. Phys. J. C* **81** (2021) 800, doi:10.1140/epjc/s10052-021-09538-2, arXiv:2104.01927.

[18] CMS Collaboration, "CMS luminosity measurement for the 2017 data-taking period at $\sqrt{s}$ = 13 TeV", CMS Physics Analysis Summary CMS-PAS-LUM-17-004, 2018.

[19] CMS Collaboration, "CMS luminosity measurement for the 2018 data-taking period at $\sqrt{s}$ = 13 TeV", CMS Physics Analysis Summary CMS-PAS-LUM-18-002, 2019.

[20] P. Nason, "A new method for combining NLO QCD with shower Monte Carlo algorithms", *JHEP* **11** (2004) 040, doi:10.1088/1126-6708/2004/11/040, arXiv:hep-ph/0409146.

[21] S. Frixione, P. Nason, and C. Oleari, "Matching NLO QCD computations with parton shower simulations: the POWHEG method", *JHEP* **11** (2007) 070, doi:10.1088/1126-6708/2007/11/070, arXiv:0709.2092.

[22] S. Alioli, P. Nason, C. Oleari, and E. Re, "A general framework for implementing NLO calculations in shower Monte Carlo programs: the POWHEG BOX", *JHEP* **06** (2010) 043, doi:10.1007/JHEP06(2010)043, arXiv:1002.2581.

[23] T. Ježo and P. Nason, "On the treatment of resonances in next-to-leading order calculations matched to a parton shower", *JHEP* **12** (2015) 065, doi:10.1007/JHEP12(2015)065, arXiv:1509.09071.

[24] J. Alwall et al., "The automated computation of tree-level and next-to-leading order differential cross sections, and their matching to parton shower simulations", *JHEP* **07** (2014) 079, doi:10.1007/JHEP07(2014)079, arXiv:1405.0301.

[25] NNPDF Collaboration, "Parton distributions for the LHC Run II", *JHEP* **04** (2015) 040, doi:10.1007/JHEP04(2015)040, arXiv:1410.8849.

[26] NNPDF Collaboration, "Parton distributions from high-precision collider data", *Eur. Phys. J. C* **77** (2017) 663, doi:10.1140/epjc/s10052-017-5199-5, arXiv:1706.00428.

[27] T. Sjöstrand et al., "An introduction to PYTHIA 8.2", *Comput. Phys. Commun.* **191** (2015) 159, doi:10.1016/j.cpc.2015.01.024, arXiv:1410.3012.

[28] P. Skands, S. Carrazza, and J. Rojo, "Tuning PYTHIA 8.1: the Monash 2013 tune", *Eur. Phys. J. C* **74** (2014) 3024, doi:10.1140/epjc/s10052-014-3024-y, arXiv:1404.5630.

[29] CMS Collaboration, "Event generator tunes obtained from underlying event and multiparton scattering measurements", *Eur. Phys. J. C* **76** (2016) 155, doi:10.1140/epjc/s10052-016-3988-x, arXiv:1512.00815.

[30] CMS Collaboration, "Extraction and validation of a new set of CMS PYTHIA8 tunes from underlying-event measurements", *Eur. Phys. J. C* **80** (2020) 4, doi:10.1140/epjc/s10052-019-7499-4, arXiv:1903.12179.

[31] GEANT4 Collaboration, "GEANT4—a simulation toolkit", *Nucl. Instrum. Meth. A* **506** (2003) 250, doi:10.1016/S0168-9002(03)01368-8.

[32] CMS Collaboration, "Measurement of the inelastic proton-proton cross section at $\sqrt{s} = 13$ TeV", *JHEP* **07** (2018) 161, doi:10.1007/JHEP07(2018)161, arXiv:1802.02613.

[33] CMS Collaboration, "Particle-flow reconstruction and global event description with the CMS detector", *JINST* **12** (2017) P10003, doi:10.1088/1748-0221/12/10/P10003, arXiv:1706.04965.

[34] CMS Collaboration, "Performance of photon reconstruction and identification with the CMS detector in proton-proton collisions at $\sqrt{s} = 8$ TeV", *JINST* **10** (2015) P08010, doi:10.1088/1748-0221/10/08/P08010, arXiv:1502.02702.

[35] M. Cacciari, G. P. Salam, and G. Soyez, "The anti-k_{T} jet clustering algorithm", *JHEP* **04** (2008) 063, doi:10.1088/1126-6708/2008/04/063, arXiv:0802.1189.

[36] M. Cacciari, G. P. Salam, and G. Soyez, "FastJet user manual", *Eur. Phys. J. C* **72** (2012) 1896, doi:10.1140/epjc/s10052-012-1896-2, arXiv:1111.6097.

[37] E. Bols et al., "Jet flavour classification using DeepJet", *JINST* **15** (2020) P12012, doi:10.1088/1748-0221/15/12/P12012, arXiv:2008.10519.

[38] CMS Collaboration, "Performance summary of AK4 jet b tagging with data from proton-proton collisions at 13 TeV with the CMS detector", CMS Detector Performance Note CMS-DP-2023-005, 2023.

[39] CMS Collaboration, "Performance of missing transverse momentum reconstruction in proton-proton collisions at $\sqrt{s} = 13$ TeV using the CMS detector", *JINST* **14** (2019) P07004, doi:10.1088/1748-0221/14/07/P07004, arXiv:1903.06078.

[40] CMS Collaboration, "Technical proposal for the Phase-II upgrade of the Compact Muon Solenoid", CMS Technical Proposal CERN-LHCC-2015-010, CMS-TDR-15-02, 2015.

[41] M. J. Oreglia, "A study of the reactions $\psi' \to \gamma\gamma\psi$". PhD thesis, Stanford University, 1980. SLAC-R-236.

[42] J. E. Gaiser, "Charmonium Spectroscopy from Radiative Decays of the J/ψ and ψ'". PhD thesis, Stanford University, 1982. SLAC-R-255.

[43] R. A. Fisher, "On the interpretation of χ^2 from contingency tables, and the calculation of P", *J. R. Stat. Soc.* **85** (1922) 87, doi:10.2307/2340521.

[44] P. D. Dauncey, M. Kenzie, N. Wardle, and G. J. Davies, "Handling uncertainties in background shapes: the discrete profiling method", *JINST* **10** (2015) P04015, doi:10.1088/1748-0221/10/04/P04015, arXiv:1408.6865.

[45] T. Junk, "Confidence level computation for combining searches with small statistics", *Nucl. Instrum. Meth. A* **434** (1999) 435, doi:10.1016/S0168-9002(99)00498-2, arXiv:hep-ex/9902006.

[46] A. L. Read, "Presentation of search results: the CL_s technique", *J. Phys. G* **28** (2002) 2693, doi:10.1088/0954-3899/28/10/313.

[47] ATLAS and CMS Collaborations, and LHC Higgs Combination Group, "Procedure for the LHC Higgs boson search combination in Summer 2011", Technical Report CMS-NOTE-2011-005, ATL-PHYS-PUB-2011-11, 2011.

[48] G. Cowan, K. Cranmer, E. Gross, and O. Vitells, "Asymptotic formulae for likelihood-based tests of new physics", *Eur. Phys. J. C* **71** (2011) 1554, doi:10.1140/epjc/s10052-011-1554-0, arXiv:1007.1727. [Erratum: doi:10.1140/epjc/s10052-013-2501-z].

[49] CMS Collaboration, "The CMS statistical analysis and combination tool: COMBINE", 2024. arXiv:2404.06614. Submitted to *Comput. Softw. Big Sci.*